Published online 5 July 2021

Nucleic Acids Research, 2021, Vol. 49, No. 13 ***7753–7764***
https://doi.org/10.1093/nar/gkab562

NMR structure of the *Vibrio vulnificus* ribosomal protein S1 domains D3 and D4 provides insights into molecular recognition of single-stranded RNAs

Nusrat Shahin Qureshi†, Tobias Matzel†, Erhan Can Cetiner, Robbin Schnieders, Hendrik R. A. Jonker, Harald Schwalbe* and Boris Fürtig*

Institute for Organic Chemistry and Chemical Biology, Center for Biomolecular Magnetic Resonance (BMRZ), Johann Wolfgang Goethe-Universität, Frankfurt am Main, Hesse 60438, Germany

Received August 19, 2020; Revised June 09, 2021; Editorial Decision June 10, 2021; Accepted June 14, 2021

ABSTRACT

The ribosomal S1 protein (rS1) is indispensable for translation initiation in Gram-negative bacteria. rS1 is a multidomain protein that acts as an RNA chaperone and ensures that mRNAs can bind the ribosome in a single-stranded conformation, which could be related to fast recognition. Although many ribosome structures were solved in recent years, a high-resolution structure of a two-domain mRNA-binding competent rS1 construct is not yet available. Here, we present the NMR solution structure of the minimal mRNA-binding fragment of *Vibrio Vulnificus* rS1 containing the domains D3 and D4. Both domains are homologues and adapt an oligonucleotide-binding fold (OB fold) motif. NMR titration experiments reveal that recognition of miscellaneous mRNAs occurs via a continuous interaction surface to one side of these structurally linked domains. Using a novel paramagnetic relaxation enhancement (PRE) approach and exploring different spin-labeling positions within RNA, we were able to track the location and determine the orientation of the RNA in the rS1–D34 bound form. Our investigations show that paramagnetically labeled RNAs, spiked into unmodified RNA, can be used as a molecular ruler to provide structural information on protein-RNA complexes. The dynamic interaction occurs on a defined binding groove spanning both domains with identical β2-β3-β5 interfaces. Evidently, the 3′-ends of the cis-acting RNAs are positioned in the direction of the N-terminus of the rS1 protein, thus towards the 30S binding site and adopt a conformation required for translation initiation.

INTRODUCTION

The elucidation of bacterial ribosome structures by X-ray crystallography and cryo-electron microscopy (cryo-EM) has been key to understand the molecular basis of protein synthesis (1,2). The ribosome structures capture numerous translational intermediates and thus provide profound insight into the translation process (3–10). However, the largest ribosomal protein S1 (rS1, 61 kDa) is generally absent from ribosome structures, although it is functionally important during translation initiation. rS1 is a multi-domain protein that is divided into two functionally specialized parts that execute different tasks in the context of translation (11). In Gram-negative bacteria, rS1 typically consists of six imperfect oligonucleotide-binding fold (OB fold) repeats of approximately ∼ 75 amino acids. As often encountered in nucleic acid-binding proteins, the OB fold domains are separated by linkers of 10–15 amino acids (12,13). The two N-terminal domains (D1–D2) have lost their nucleic acids-binding ability, however. These domains are responsible for ribosome binding, where rS1 is anchored to the ribosomal protein S2 via its N-terminal unstructured region (14). The four C-terminal domains (D3–D6) of rS1 are decoupled from the N-terminus via a flexible linker and interact with the 5′-untranslated regions (5′-UTR) of mRNAs. rS1 binds various mRNAs without sequence specificity, which is in line with its anticipated role to promote translation initiation of many different RNAs, although a preference for AU-rich sequences is often observed (15,16). As an RNA chaperone rS1 stabilizes single-stranded mRNA conformations by undergoing transient RNA-protein interactions. Thus, rS1 melts secondary structure at the ribosome binding site, opening the mRNA available for further interactions essential for the start of translation (17,18). In fact, this region harbors the so-called Shine–Dalgarno (SD) sequence, which binds to the complementary anti-SD sequence within the 16S rRNA (19). There-

*To whom correspondence should be addressed. Tel: +49 69 7982 9157; Fax: +49 69 7982 9515; Email: fuertig@nmr.uni-frankfurt.de
Correspondence may also be addressed to Harald Schwalbe. Email: schwalbe@nmr.uni-frankfurt.de
†The authors wish it to be known that, in their opinion, the first two authors should be regarded as Joint First Authors.

fore, rS1 brings the mRNA transcript in the proximity of the ribosomal decoding channel, enabling fast mRNA recognition by the 30S subunit (20). Recent studies also imply an involvement of rS1 in the translational-regulation mechanism of RNA-based cis-regulatory elements termed riboswitches (21). Deletion of the rS1 coding gene *rpsa* is lethal to *E. coli* (22), emphasizing the importance of this ribosomal protein for translation in Gram-negative bacteria.

Despite its important role, structures of full-length rS1 are not available at atomic resolution, neither in the free nor in an bound state. This is mainly due to the highly dynamic behavior of rS1 that hampers structural characterization by X-ray and cryo-EM. However, as the D1–D2 domains display sufficient rigidity in the bound state, their structures are increasingly being co-elucidated either when bound to the small ribosomal subunit (14,23,24) or to the phage Qβ replicase that is known to hijack rS1 during phage infection (25,26). Although NMR solution structures of the single-domains D4 and D6 from *Escherichia coli* rS1 were reported (27), these structures lack the interplay between the adjacent domains. These interactions are exceedingly being captured in recent cryo-EM studies of ribosomal particles, in which C-terminal rS1 domains could be observed, however, at low structural resolution (23,24,28).

Recently, we showed that the rS1 from the human pathogenic bacterium *Vibrio vulnificus* displays a unique domain architecture, in which domains D3 and D4 constitute a well-folded, minimal mRNA-binding platform, whereas domain D5 is additionally needed to restore full RNA chaperoning activity of rS1 (18). Here, we present the solution NMR structure for the D3–D4 fragment (rS1–D34) of the *Vibrio vulnificus* ribosomal S1 protein. Both domains exhibit an OB-fold structure, and their RNA-binding sites are co-aligned, offering a continuous interaction platform for mRNA recognition. Our studies further show that rS1–D34 interacts with the ribosome-binding sites of various riboswitches with comparable affinities. Moreover, with substoiciometric amounts of RNAs position-specific labeled position-specifically with paramagnetic nitroxide groups, we were able to employ these RNAs as a molecular ruler to study the binding mode of the RNA, using paramagnetic relaxation enhancement (PRE) (29,30). We thus developed a novel PRE method that can be utilized for studying interactions in intermediate to fast exchanging systems, without severe signal bleaching at saturating RNA concentration.

MATERIALS AND METHODS

Sample preparation

The rS1–D34 protein sequence is as follows:

GAMETLQEGSEVKGIVKNLTDYGAFVDLGGV
DGLLHITDMAWKRVKHPSEIVNVGDEILVKVLKF
DRDRTRVSLGLKQLGEDPWVAIAKRYPEGHKL
SGRVTNLTDYGCFVEIEEGVEGLVHVSEMDWTNK
NIHPSKVVNVGDEVEVMVLEIDEERRRISLGLKQ
CKANPWQS

The rS1–D3 protein sequence is as follows:

GAMETLQEGSEVKGIVKNLTDYGAFVDLGGVD
GLLHITDMAWKRVKHPSEIVNVGDEILVKVLKFD
RDRTRVSLGLKQLGED

The rS1-D4 protein sequence is as follows:

GAMAIAKRYPEGHKLSGRVTNLTDYGCFVEIE
EGVEGLVHVSEMDWTNKNIHPSKVVNVGDEVE
VMVLEIDEERRRISLGLKQCKANPWQS

The underlined amino acids are artificial and were introduced by the vector backbone (pKMTX).

Expression and purification of ^{15}N and $^{13}C^{15}N$ labeled rS1–D3, rS1–D4 and rS1–D34 proteins was performed as described previously (18). In case of fractional deuteration of rS1–D34 the expression protocol was modified in order to adapt the cells to the desired D_2O content of 60% (v/v), in steps of 10% (v/v), 30% (v/v) and finally 60% (v/v) D_2O M9 culture. The preparative expression was carried out in 60% (v/v) D_2O M9 culture supplemented with 1 g/l ^1H, ^{15}N-NH_4Cl and 2 g/l ^1H, ^{13}C-glucose.

Unmodified 14mer RNAs were purchased from Dharmacon Inc., deprotected and desalted according to the protocol of the manufacturer. Freeze-dried RNAs were reconstituted in NMR buffer (25 mM potassium phosphate (pH 7.2), 150 mM KCl and 5 mM DTT).

The 2′-amino-modified 14mer RNAs were purchased from Dharmacon Inc., deprotected according to the manufacturer's protocol and purified by HPLC, using 0.1 M Triethylammonium acetate (pH 6.1) buffer. The HPLC buffer was removed with four freeze-dry cycles using water as solvent, because the Triethylamine hampers the subsequent spin-labeling reaction. The synthesis of the spin-label and the spin-labeling reaction were carried out according to the protocol by Edwards *et al*. (31). Integrity of the spin labeled RNA was evaluated by using MALDI-mass spectrometry.

NMR spectroscopy

NMR experiments were acquired on protein samples (up to 1.5 mM concentration) in a buffer containing 25 mM potassium phosphate (pH 7.2), 150 mM KCl and 5 mM DTT. The samples contained 5 to 10% (v/v) D_2O and usually 100 μM Trimethylsilylpropanoic acid (TSP) as internal chemical shift standard. Nitrogen and carbon chemical shifts were indirectly referenced, using the chemical shift referencing ratios $^{13}C = 0.25144953$ and $^{15}N = 0.101329118$ (32). Spectra were acquired on Bruker spectrometer (600, 700, 800, 900 and 950 MHz) equipped with ^1H, $\{^{13}C; ^{15}N\}$ triple resonance cryogenic probes. Standard Bruker pulse sequences (Topspin 3.5) were used. All spectra were processed with Topspin 3.5 and analyzed with Sparky 3.114 (33). All assignment experiments were acquired at 303 K, typically using BEST sequences and non-uniform sampling technique to improve spectral quality and to reduces the experimental time (34–36).

Sequential backbone assignment was achieved with BEST-TROSY-based 3D NMR experiments including HN-CACB, HN(CO)CACB, HNCO, HN(CA)CO, HNCA and HN(CO)CA. Aliphatic sidechains were assigned with H(CC)(CO)NH, (H)CC(CO)NH and HCCH-TOCSY experiments. The chemical shift assignment was further complemented using 3D HNHA, 3D ^1H, ^1H, ^{15}N-NOESY-HSQC (mixing time 100 ms) and aliphatic and aromatic 3D ^1H, ^1H, ^{13}C-NOESY-HSQCs (mixing time 120 ms).

Residual dipolar couplings (RDCs) were measured on ∼300 μM ^{15}N–rS1–D34 samples at 600 MHz and 303 K. ^1H, ^{15}N-(IPAP)-HSQC experiments were used to mea-

sure ^{1}J(N, H) coupling constants under isotropic and anisotropic conditions. Partial alignment of the protein molecules was achieved by using either filamentous Pf1-phages (3.6 mg/ml, *Pseudomonas aeruginosa*, strain LP11-92, ASLA Biotech, Latvia) or stretched polyacrylamide gels (PAA, 4.5%, v/v). In case of Pf1-alignment, phages were extensively exchanged against NMR buffer using centrifugal concentrators (VivaSpin2, Sartorius, Germany; MWCO 10 kDa) and were subsequently titrated into the NMR sample (300 μM ^{15}N–rS1–D34 in 25 mM potassium phosphate (pH 7.2), 150 mM KCl, 5 mM DTT, 3.6 mg/ml Pf1) until an HDO splitting of 7 Hz was observed. Gel-alignment was obtained by mechanically stretching protein-soaked (300 μM) PAA gels, using the Gel Kit from New Era Enterprises Inc. (USA). The gel was pressed into a Gel sample tube (open at both ends) and sealed with the provided plugs. The pushing through the Gel Press led to a change in gel-diameter from 6 to 4.2 mm, inducing an HDO splitting of 2 Hz.

The ^{15}N-relaxation data (R_1, R_2 and {^{1}H}, ^{15}N-heteronuclear NOE (HetNOE)) were acquired on a ^{15}N-labeled rS1–D34 sample (250 μM) at 600 MHz and 308 K. T_1 and T_2 relaxation times were acquired as pseudo 3D experiments using temperature compensated pulse sequences as distributed in Topspin 3.5. Longitudinal relaxation times were determined from a series of spectra with the delays 100, 200, 400, 600, 800, 1200 and 3000 ms. In case of transverse relaxation times the delays 16.96, 33.92, 67.84, 101.76, 135.68 and 271.36 ms were used. The relaxation times were transformed into relaxation rates using the following equations:

$$R_1 = \frac{1}{T_1} \text{ and } R_2 = \frac{1}{T_2}$$

HetNOE data were acquired as interleaved 2D experiments. Rotational correlation times (τ_c) were determined on the basis of relaxation data with the TENSOR 2.0 program (37). Theoretical values were estimated by hydrodynamic calculations using HydroNMR (38).

Temperature series were acquired as ^{1}H, ^{15}N-HSQC experiments at 600 MHz, using temperatures ranging from 289 to 313 K with 2 K increments.

NMR titration experiments were performed at 308 K on 100 μM ^{15}N–rS1–D34 samples, to which the RNAs were stepwise added in molar ratios ([RNA]:[protein]) of 0, 0.1, 0.2, 0.3, 0.6, 1, 2, 4 and 5.5. Chemical shift perturbations (CSPs) were calculated as Euclidian distances using:

$$\text{CSP}\,(\Delta\delta_{\text{HN}}) = \sqrt{(0.1\Delta\delta_{\text{N}})^2 + (\Delta\delta_{\text{H}})^2}$$

Dissociation constants were extracted by plotting CSPs as function of RNA concentration and fitting according to (39):

$$\Delta\,\delta_{\text{obs}} = \Delta\delta_{\text{max}} \left\{ \frac{([P]_0 + [R]_0 + [K_{\text{D}}]) - \sqrt{([P]_0 + [R]_0 + [K_{\text{D}}])^2 - 4[P]_0[R]_0}}{2[P]_0} \right\}$$

Paramagnetic relaxation enhancement (PRE) experiments were carried out with ^{15}N–rS1–D34 (100 μM) in 3 mm diameter NMR tubes at 308 K and 313 K at 600 MHz. The ^{1}H,^{15}N-HSQC-based pulse sequence published by Iwahara *et al.* was used (40). For interaction studies the paramagnetic relaxation delay was optimized to 8 ms testing a set of delays (4.8, 6, 10, 12, 14, 18 and 22 ms; Supplementary Figure S1).

Structure calculation

The structure calculations were based on 3D ^{1}H,^{1}H,^{13}C-NOESY-HSQC (aromatic and aliphatic, both in 100% (v/v) D_2O) and ^{1}H,^{15}N-NOESY-HSQC spectra using mixing times of 120 ms and 100 ms, respectively. The peaks in the 3D spectra were picked based on the respective 2D HSQC spectra using the restricted peak picking command (kr) in Sparky version 3.114 (33). They were manually inspected for peak picking artefacts and subsequently used for structure calculation employing the software package CYANA (41,42). In CYANA version 3.97, the automated NOE cross peak assignment routine was used for assignment of the NOESY signals. The chemical shift tolerances were set to 0.015 ppm for the directly bound protons, to 0.025 ppm for all other protons and to 0.2 ppm for hetero atoms. In addition, hydrogen bonds (validated by NOE assignments, hydrogen/deuterium exchange experiments (Supplementary Figure S2). and initial structure calculations), dihedral angle restraints (as predicted by TALOS-N (43) and validated by initial structure calculations), ^{3}J(H^N, H^α) coupling constants (calculated from 3D HNHA) as well as ^{1}D (HN) residual dipolar couplings (gel-aligned and Pf1-aligned) were included for structure determination. A total of 100 structures per iteration cycle were calculated using 15000 refinement steps. The 20 lowest-energy structures were analyzed and refined in explicit water using ARIA protocols (44). The two sets of residual dipolar couplings were examined in PALES (45), yielding correlation coefficients of the magnitude 0.953 (Pf1-aligned) and 0.971 (gel-aligned).

RESULTS

NMR resonance assignment and dynamics of rS1–D34

The resonance assignment of the 173 amino acid long rS1–D34 fragment (19.4 kDa) was achieved using standard 3D experiments (HNCACB, HN(CO)CACB, HNCO, HN(CA)CO, HNCA, HN(CO)CA HNHA, H(CC)(CO)NH, (H)CC(CO)NH, HCCH-TOCSY). The experiments were performed on a fractionally deuterated and uniformly ^{13}C- and ^{15}N-labeled sample to assure assignment completeness. In addition, 3D NOESY-HSQCs were acquired, for which either a uniformly ^{15}N-labeled or a uniformly ^{13}C- and ^{15}N-labeled sample was used. All observed resonances in the ^{1}H,^{15}N-HSQC were assigned (Figure 1A), corresponding to 95% of the expected backbone amide resonances. Backbone amide signals from amino acids D249, T253, A269, K314, L346 and C349 were not observed in the ^{1}H,^{15}N-HSQC. However, their side chain chemicals shifts were assigned in the aliphatic ^{1}H,^{13}C-HSQC.

The backbone dynamics (Figure 1B) as probed by R_1, R_2 and {^{1}H}, ^{15}N-heteronuclear NOE (HetNOE) experiments display rigidity for the folded core and increased flexibility for terminal residues as well as for residues residing in the middle of both L_{34} loops and at the beginning of the inter-domain linker. The backbone dynamics are similar for both

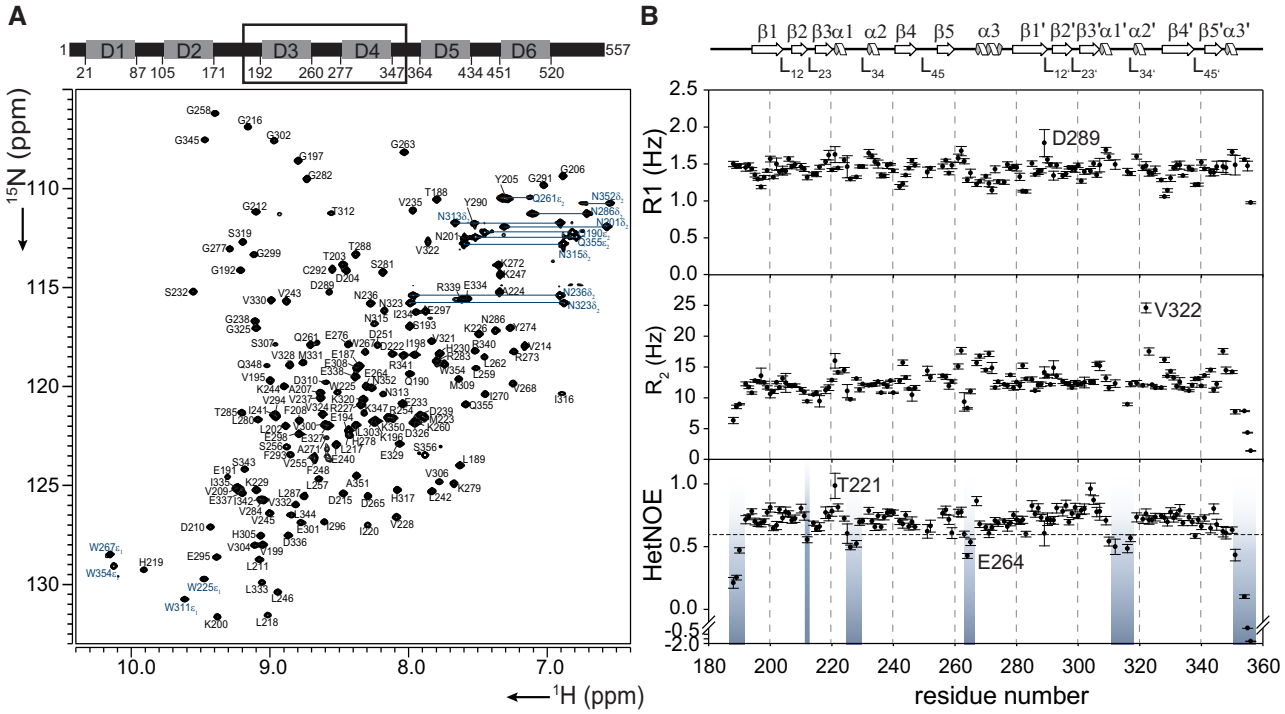

Figure 1. Resonance assignment and backbone dynamics of rS1–D34. (**A**) The ^{1}H,^{15}N-HSQC spectrum of ^{15}N–rS1–D34 (1.3 mM) was acquired at 950 MHz and 303 K in 25 mM potassium phosphate (pH 7.2), 150 mM KCl, 5 mM DTT, 5% D_2O. The resonance assignment is annotated. Side chain NH resonances are assigned in blue. The backbone amide resonance of T221 is not visible at the given contour level. A schematic of the rS1 is shown on top. The rS1–D34 region is indicated with a box. (**B**) R_1, R_2 and $\{^{1}H\}$, ^{15}N heteronuclear NOE experiments were acquired at 308 K and 600 MHz on a 250 μM ^{15}N-labeled rS1–D34 sample. Relaxation rates and HetNOE values are given as function of protein sequence. Ambiguous resonances were excluded. Secondary structure elements are shown on the top and were predicted with TALOS-N (43). Flexible regions (HetNOE < 0.6, below black dashed line) are highlighted with blue boxes.

domains, demonstrating that they tumble together as one unit on a sub-τ_c time scale. In line, the rotational correlation time determined for the whole rS1–D34 protein (τ_c = 8.8 ns) agrees with the values calculated for separate domains (rS1–D34^{NTD}: τ_c = 8.6 ns and rS1–D34^{CTD}: τ_c = 7.5 ns) and further agrees with the predicted value from HydroNMR (τ_c = 10.3 ns) (38). The predicted values for the isolated domains are about two-folds lower (D3: τ_c = 4.0 ns, D4: τ_c = 5.2 ns; model structure of single domains used for HydroNMR calculation (38,46)), again demonstrating that both domains are structurally linked and do not tumble independently from each other in the two domain construct rS1–D34. The inter-domain linker that spans from Q261 to E276 overall displays HetNOE values above 0.6, with a local minimum (∼0.4) around E264, suggesting a predominantly rigid inter-domain linker with a local dynamic joint to domain D3.

Structural analysis of rS1–D34

For structure calculation, 8319 peaks were extracted from the ^{1}H,^{15}N-NOESY-HSQC and the two ^{1}H,^{13}C-NOESY-HSQCs (aliphatic and aromatic), using restricted peak picking in Sparky 3.114 (33). 6029 cross peaks were assigned with the automated NOESY assignment routine in CYANA 3.97 and a total of 4217 NOE-based distance restraints were extracted (42). Further, 42 main chain hydrogen bond restraints were inferred from observed NOESY cross peak patterns and altogether 321 dihedral angles were extracted from TALOS-N (43). In addition, 224 residual dipolar couplings (measured in phages and gel) and 71 $^{3}J(H^{N},H^{\alpha})$ scalar couplings were included in the structure calculation (Table 1).

The solution NMR structure (Figure 2) shows similar topologies for both domains. Each S1 domain contains five β-strands (β1–β5 in D3 and β1′–β5′ in D4) that are typically separated by short loops (∼four amino acids). Between strands β3 and β4 a long loop (L_{34} ∼ 18 amino acids) is found that displays short α-helical regions at its termini. Both S1 domains are separated by two consecutive α-helices stretching from K260 to L262 and P266 to R273. Between these two helices, a dynamic joint is found that resides around E264.

In early structure calculations the folded core of both domains exhibited tight structure bundles with RMSDs ranging between 1 and 2 Å but The relative domain orientation could not be established. Presumably, the flexibility of the dynamic joint within the inter-domain linker led to scarce NOE data. This flexibility might stem from dynamics slower than the overall rotational tumbling, as it is not evident from analysis of ^{15}N relaxation data. Only a few contacts between the two domains could be derived from NOESY experiments, in which common cross peaks were observed to the inter-domain linker. For instance, we observed NOEs between the L_{34} linker of domain D3 (residues including and flanking W225) to the inter-domain linker (residues includ-

Table 1. Structural statistics for the ensemble of the 20 top ranked structures of rS1–D34

Experimental restraints	
NOE distances	
Total	4217
Intra residual (i-j = 0)	849
Sequential (i-j = 1)	1040
Medium range (1<i-j<5)	642
Long range (i-j≥5)	1686
Hydrogen bonds	42
Dihedral angles (Φ/Ψ)	321
Scalar couplings ($^3J(H^N,H^\alpha)$)	71
Residual dipolar couplings	
$^1D(N,H)$; gel-aligned	101
$^1D(N,H)$; Pf1	123
Ramachandran plot[a]	
Most favored	82.4%
Additionally allowed	17.5%
Generously allowed	0.1%
Disallowed	0.0%
Average RMSD to mean (Å)[b]	
All heavy atoms	1.03 ± 0.23
All backbone	0.70 ± 0.25
Selected heavy atoms (G^{192}-K^{347})	0.78 ± 0.08
Selected backbone (G^{192}-K^{347})	0.35 ± 0.06

[a]Calculated with PROCHECK, excluding glycines and prolines.
[b]Calculated with MOLMOL2k2.

ing and flanking W267). However, the overall interaction interface between D3 and D4 was poorly described and thus their relative orientation could not be fixed by NOE-derived restraints. Therefore, RDC-based restraints were crucial for convergence during structure calculation. In the solution structure both domains were co-aligned, where the RNA binding sites of the two domains faced the same direction, inducing a continuous interaction surface for RNA binding.

Previously, we postulated that the sidechain-sidechain interaction between the domain tryptophan W225 and the linker tryptophan W267 stabilized individual domains (18). Although the rS1–D34 solution structure does not reveal direct interaction between the two sidechains, we find that the two tryptophan sidechains are placed spatially close to each other and probably contribute to structure and rigidity of the inter-domain linker. For instance, we observe hydrogen-bonding of the indole NH of W225 to either the backbone carbonyl of K260 or the carboxyl moiety of D265 in a subset of structures within the bundle. Both amino acids reside within the inter-domain linker. Although this interaction probably rigidifies the inter-domain linker, we do observe dynamics within this region. In fact, temperature-dependent $^1H,^{15}N$-HSQC spectra indicate a conformational transition, where for A224 and Q261 nonlinear movements of temperature-dependent chemical shifts are observed (Supplementary Figure S3).

rS1–D34 binding to SD regions of translational riboswitches

We previously reported the RNA-binding behavior of rS1–D34 to the 5′-UTR of the *V. vulnificus adenosine deaminase (add)* gene that comprises the translation-regulating adenine-sensing riboswitch (Asw). This riboswitch contains a rather weak SD sequence (ΔG = –1.4 kcal/mol, see Table 2 and Supplementary Figure S4) and likely requires the rS1 protein for productive translation. We wondered whether the rS1 protein also binds to the SD region of other riboswitches with similar affinities and whether the RNA binding is modulated by the strength of the SD sequence. Therefore, we chose four additional translational riboswitches (see Table 2) as rS1 targets: the hydroxocobalamin (HyCbl)-sensing riboswitch, two classes (I and III) of the 7-aminomethyl-7-deazaguanine (preQ1)-sensing riboswitches and the thiamine pyrophosphate (TPP)-sensing riboswitch (47–50). The RNAs were selected in order to probe a broad range of SD-strengths, ranging from ΔG = –1.4 kcal/mol to ΔG = –12.2 kcal/mol (see Table 2 and Supplementary Figure S4) and covered a length of 14 nucleotides. As a negative control, we included a 14 nt long model hairpin containing an artificial SD sequence (GAAG) residing in its tetraloop.

The RNA binding affinities were measured by NMR titration experiments, with stepwise addition of unlabeled RNA to ^{15}N-labeled rS1–D34 protein and acquisition of $^1H,^{15}N$-BEST-TROSY experiments for each titration step (Table 2). The SD-regions of the preQ1(III) and the HyCbl riboswitch display comparable apparent dissociation constants (K_D (preQ1(III)-14) = 7 ± 4 μM; K_D (HyCbl-14) = 13 ± 4 μM) as were found for the adenine-sensing riboswitch, whereas the TPP-14 RNA exhibits a ∼3-fold lower affinity (K_D (TPP-14) = 33 ± 6 μM). By contrast, low affinities were observed for RNAs that exhibit stable secondary structures. Although preQ1(I)-14 contains the strongest SD-sequence it is bound with low affinity as it oligomerizes into a G-quadruplex structure (Supplementary Figure S5). Similarly, no binding was detected for the model hairpin, as it forms a stable secondary structure which does not exhibit any rS1-binding site. The NMR titration experiments further revealed that the RNA-binding site on rS1–D34 is conserved for the different RNA constructs (Figure 3). In particular, Y205, R252, R254 in domain D3 as well as Y290, F293 and R341 in domain D4 are involved in RNA binding. Additionally, amino acids (e.g. I220 and E301) that reside in the primary contact surface exhibit large CSPs. These changes are indicative of conformational changes upon complex formation. Intriguingly, the binding interface displays a predominantly positively charged surface that is confined to one side of the rS1–D34 structure spanning both domains (Supplementary Figure S6). In fact, comparative RNA binding studies with the single domain constructs rS1–D3 and rS1–D4 hinted at cooperative binding of RNA, further underlining the necessity of both domains for productive RNA binding (Supplementary Figure S7). Especially domain D3 seemed to be essential for stable RNA binding, partially also because this domain stabilizes the whole mRNA binding region of rS1, as we reported previously (18).

Further, the aromatic and basic patches are segregated on the top (e.g. Y205) and on the bottom (e.g. R254) of the domains within each barrel structure (Figure 2C, see also Supplementary Figure S6). As a direct consequence, domains D3 and D4 form an extended groove that accommodates the RNA strand, where the negatively charged sugar-

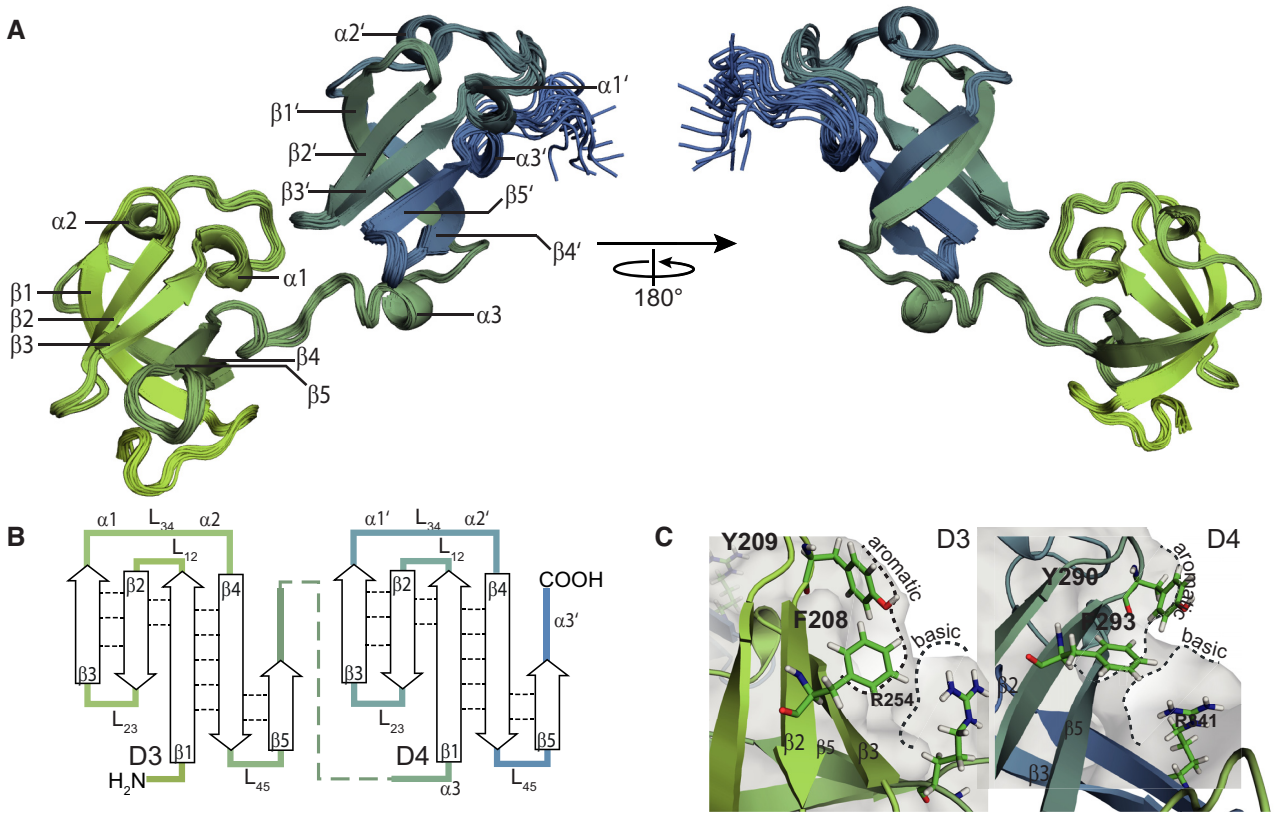

Figure 2. NMR solution structure of rS1–D34. (**A**) Ensemble of 20 lowest-energy structures is shown with view on the RNA-binding interface (β2–β3–β5). The protein is represented as cartoon and color coded from N- (green) to C-terminus (blue). In the right panel the protein is rotated by 180°. (**B**) The topology of each domain is depicted and color coded. (**C**) Enhanced view of each domain is shown with focus on the RNA binding interface. The interacting residues are displayed.

phosphate backbone is placed spatially close to arginine residues, and the nucleobases to the tyrosines. Within this groove, the RNA strand can bind if a minimal length of 14nt is provided. These findings are in line with earlier studies that experimentally determined an rS1:RNA ratio of 1:2–3 for oligonucleotides as small as 5 nt that increased to equimolar binding at length between 9 and 30 nt. For larger RNAs with 30 - 80nt, the binding stoichiometry rS1:RNA is greater (51).

Taken together, the rS1–D34 showed dissociation constants in the lower μM range for binding to SD regions of different translational riboswitches. To further dissect the influence of SD-strength on rS1-binding, we systematically mutated the rather strong, G-rich SD sequence of HyCbl-14 (AA**GGAGA**, $\Delta G = -8.5$ kcal/mol,) to weaker SD sequences ($\Delta G \sim -2$–3 kcal/mol), yielding altogether six HyCbl-14 variants (see Table 2 and Supplementary Figure S4). In these mutants, we stepwise mutated the initial guanine nucleotides G10, G11 and G13 to either purine (A) or pyrimidine (C) containing nucleotides. Modulations in binding affinities were assessed by NMR titration experiments (Table 2).

We find that G to A mutations do not notably affect rS1–D34 binding, as the dissociation constants are in the same range (K_D = 13–15 μM) as for the wildtype HyCbl-14 RNA (K_D = 13 μM). By contrast, exchanging G to C leads to a three-fold decrease in dissociation constants (K_D = 5–8 μM) when compared to the wildtype sequence. From these findings we conclude that nucleotide type (purine vs. pyrimidine) is important for productive interactions with rS1.

A novel PRE approach to study RNA orientation in intermediate-exchanging systems

To probe the binding mode of single-stranded RNAs towards the minimal binding platform of rS1, we utilized PRE experiments.(40). In these experiments, four different spin-labeled RNAs were added to ^{15}N-labeled rS1–D34 protein samples. In case of weak binding, the free and the bound states undergo fast exchange, leading to short residence times of the paramagnetic species within the complex and resulting in multiple binding events during the timeframe of the NMR experiment. As direct consequence, the global interaction surface is mapped via several short-lived encounters. By contrast, higher affinities (K_D < 10 μM) generally lead to longer lifetimes of the complex, allowing exact localization of the paramagnetic species and further shed light on the orientation of the paramagnetic species in the complex (52). In these cases, the exchange rates between the free and bound form are slowed down to slow exchange conditions, in which the complex does not dissociate during the

Table 2. Investigated RNA constructs. The SD sequence regions are shown in bold letters. The regions were optimized to minimize dimerization. Free energies were calculated on the RNAstructure web server provided by the Matthews lab from the University of Rochester Medical center, New York (https://rna.urmc.rochester.edu/RNAstructureWeb/; 05.03.2021). Dissociation constants were determined by NMR titration experiments with rS1–D34 and were performed at 308 K. Mutations of HyCbl-14 are underlined in the HyCbl-14 variants

RNA	Organism	Sequence (5′-3′)	UC (%)	$\Delta G^{16S\ rRNA}$ (kcal/mol)[a]	$K_D^{(rS1–D34)}$ (μM)
preQ1(III)-14	*Faecalibacterium prausnitzii*	**GGAG**UAUUGUUAUG	43	− 5.9	7 ± 4
Asw-14[b]	*V. vulnificus*	**GAAG**ACUCAUGAAU	36	− 1.4	12 ± 1
HyCbl-14	Marine metagenome	AACGAGC**AAGGAGA**	14	− 8.5[c]	13 ± 4
HyCbl-14-CGAG	Marine. metagenome	AACGAGC**AACGAGA**	21	− 3.0[c]	8 ± 1
HyCbl-14-CCAG	Marine. metagenome	AACGAGC**AACCAGA**	29	− 2.2[c]	5 ± 1
HyCbl-14-CCAC	Marine. metagenome	AACGAGC**AACCACA**	36	− 2.2[c]	5 ± 1
HyCbl-14-AGAG	Marine. metagenome	AACGAGC**AAAGAGA**	14	− 2.9[c]	13 ± 1
HyCbl-14-AAAG	Marine. metagenome	AACGAGC**AAAAAGA**	14	− 2.2	14 ± 1
HyCbl-14-AAAA	Marine. metagenome	AACGAGC**AAAAAAA**	14	− 2.2[c]	15 ± 2
TPP-14	*E. coli*	**GGAA**UGAGCUAUGU	36	− 3.9	33 ± 6
(preQ1(I)-14)	*Thermoanareobacter tengcongensis*	AAAACAA**GGGAGGU**	14	− 12.7	>1000[d]
14mer	Model hairpin	GGCAC**GAAG**GUGCC	36	n.a.[c]	>1000

[a]Calculated for 37°C using host-specific 16S rRNA sequences.
[b]Reported in (16).
[c]Calculated against *V. vulnificus* 16S rRNA sequence.
[d]G-quadruplex formation.

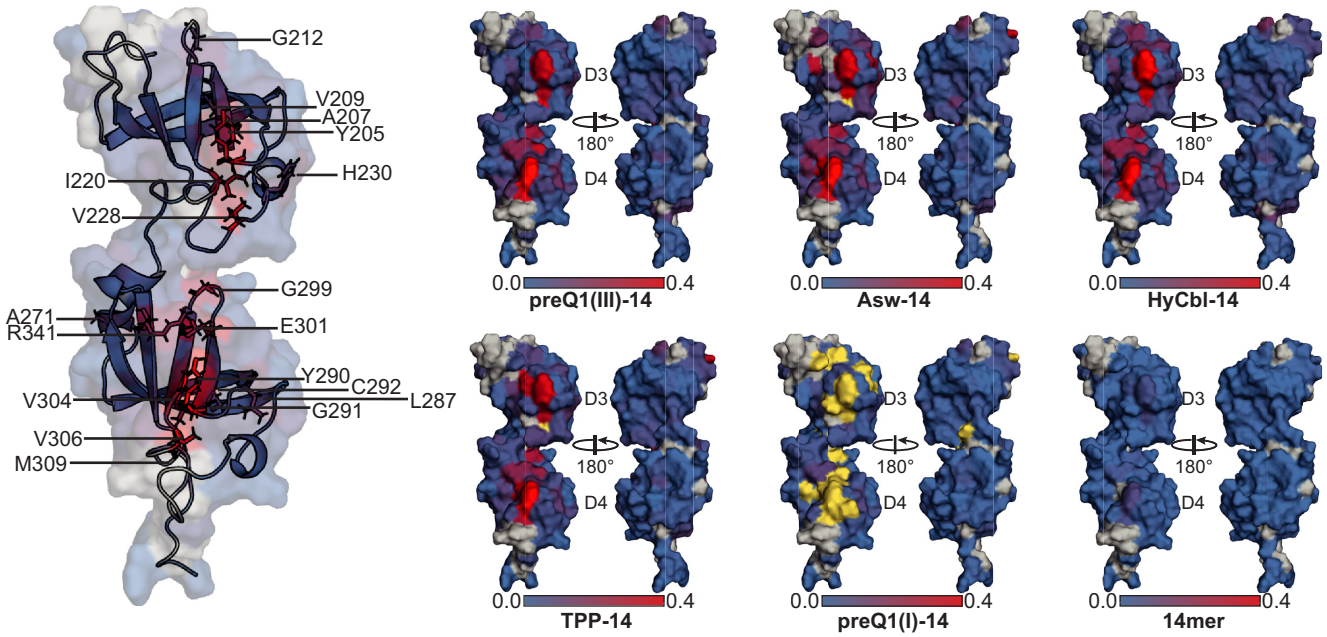

Figure 3. CSP mapping on rS1–D34 structure of all 5′-UTRs. The CSPs are color coded from blue (no CSP) to red (maximal CSP). Resonances under intermediate exchange conditions are shown in yellow. Enlarged structure in presence of 5.5 eq preQ1-(III)-14 is shown on the left-hand side in cartoon representation and transparent surface. Interacting amino acids are annotated. Maximal CSPs cluster around the same region for different RNAs. In case of preQ1(I)-14, response to increased concentration of RNA could not be observed after addition of the first RNA equivalent. With 5.5 eq RNA at a protein concentration [100 uM], no saturation could be achieved. This RNA oligomerizes to form G-quadruplex structures. At this stoichiometry, the key interacting residues (e.g. Y205/Y290) were not detected, as they were under intermediate exchange conditions.

NMR timeframe. The affinity of rS1–D34 towards the investigated RNAs, however, is around 10 μM, rendering the interaction under intermediate exchange conditions, when using (sub-)stoichiometric ratios. Such affinity regimes are difficult to tackle with paramagnetic NMR since here the PRE is not the sole source for intensity variations of the observed NMR signal. In fact, the rS1–D34 backbone amide signals display exchange-induced line-broadening upon interaction with RNA (Supplementary Figure S8). This line-broadening is particularly severe in the early course of the titration, but signals can be recovered at excess of diamagnetic RNA. At excess of paramagnetic RNA, however, the bleaching effects of the paramagnetic center are severe, preventing any meaningful data analysis (Supplementary Figure S9).

Thus, the dynamics of the rS1–D34/RNA interaction prompted us to develop an experimental approach different to existing protocols for PRE measurements. We first coun-

teracted the effect of exchange-induced line-broadening by exploiting fast-exchange signal narrowing using (i) higher temperatures (313 K instead of 308 K) and (ii) an excess of RNA (4 eq). As for (i) the higher temperature significantly improved spectral quality (Supplementary Figure S10). In order to reduce the bleaching effect caused by excess of the paramagnetic species, we conducted the PRE experiments with spiked RNA samples. We decided to add four equivalents of RNA in total while only 10% of the RNA was paramagnetic. As a diamagnetic reference, four equivalents of the corresponding unmodified RNA were added to the protein. The validity of using unmodified RNA as a diamagnetic reference was shown by ITC experiments, in which similar dissociation constants of 28 ± 2 μM for the unmodified RNA and 34 ± 3 μM for the spin-labeled RNA were determined (see Supplementary Figure S11). Incorporation of the spin label was validated by mass spectrometry (see Supplementary Figure S12).

With having a PRE method at hand that allows studying intermediate-exchanging systems, we wondered whether the affinity regime allows to determine the RNA orientation within the complex. In order to assemble complementary structural information, we employed four spin labeled RNAs. Firstly, to probe the effect of K_D on the PRE experiments we chose RNAs that displayed either the highest (preQ1(III)-14 and HyCbl-14) or the lowest (14mer model hairpin) affinities towards the rS1–D34 protein. Secondly, we employed different spin-labeling positions within the RNAs. The variation of spin-labeling position allowed us to use the RNA as a molecular ruler, providing insights on the RNA-orientation within the protein–RNA complex. In order to prevent a reduced PRE effect, we did not label the 5′ and 3′ terminal ends of the RNA, as in these cases the introduction of a spin label could decrease the residence times of the spin-labeled nucleotide in the RNA-protein complexes due to end fraying effects leading to locally increased internal dynamics.

All PRE experiments were performed with ^{15}N-labeled rS1–D34 protein and four equivalents of a 9:1 mixture of unmodified/paramagnetic RNA. The experiment with the RNA that exhibits its label closest to the 5′-end (HyCbl-3-(4-isocyanato TEMPO)) (Figure 4A) shows a complete reduction of signal intensities for residues R227 and V228 and a significant reduction of over 70% for E301. Highlighted in the structure, it becomes clear that those three amino acids are located between the two domains, indicating that the spin-label is placed in this region. To confirm these results, we chose to take another RNA sequence (preQ1-III-5-(4-isocyanato TEMPO)) and labeled the RNA close to the 5′-end at position 5(Figure 4B). Again, the residues R227, V228, and E301 were strongly affected by the PRE and show complete signal reductions in the ^{1}H,^{15}N-HSQC experiment confirming the results of HyCbl-3(4-isocyanato TEMPO).

When moving the spin-label position within the RNA to the 3′-end, the picture looks different. In the case of preQ1-III-10-(4-isocyanato TEMPO) (Figure 4, C), the strongest changes can be observed for the amino acids D204, Y205, D215 and V228 which are exclusively located within domain D3, close to the N-terminus. In contrast to the previous experiments with preQ1-III-5-(4-isocyanato TEMPO) and HyCbl-3-(4-isocyanato TEMPO), no significant effects were observed for amino acids stemming from domain D4. Overall, the intensities are less influenced by the PRE when compared to the experiment with preQ1-III-5-(4-isocyanato TEMPO).

As a negative control (Figure 4D) we used a spin-labeled RNA which forms a stable hairpin structure (14mer-11-(4-isocyanato TEMPO)) and is therefore unable to bind to the protein. As expected, no significant changes in the signal intensities were observed for this construct.

In conclusion, Figure 4 illustrates that shifting positions of the spin-label from the 5′-end to the 3′-end within the RNA induces PRE on the protein, where the intensity variations move from the C- to the N-terminus. Therefore, the OB folds of rS1 bind RNAs with standard polarity as defined in (53).

DISCUSSION

Protein synthesis is fundamental to all organisms and peptide bond formation is catalyzed by a macromolecular machinery: the ribosome. In the last fifty, years ribosomes were and continue to be in the focus of many biological and structural studies. Each new ribosome structure provides new insights into the mode of action of the ribosome. However, the rS1 protein can usually not be captured in those structures since its mRNA-binding domains display increased dynamics and the lack of structural information for this very important ribosomal protein is rather sobering. Although NMR solution structures for the isolated domains D4 (PDB entry: 2KHI) and D6 (PDB entry: 2KHJ) from *E. coli* rS1 were reported (27) and subsequently used by Beckert *et al*. to model the mRNA-binding domains in their published cryo-EM study of hibernating ribosomes (28), a high resolution structure of two OB folds in tandem forming the mRNA-binding domain is missing. This prompted us to solve the structure of the two well-folded mRNA-binding domains D3 and D4 from *Vibrio vulnificus* rS1 that together represent a minimal RNA-binding construct in this human-pathogenic bacterium. To our knowledge there is no high-resolution structure available for these mRNA-binding domains so far. We determined the NMR solution structure of rS1–D34 at an average RMSD to mean of 0.78 ± 0.08 Å for the folded core (G192-K347). In this structure the RNA-binding β-sheets (β2–β3–β5) of both domains face the same direction, comprising a continuous interaction surface for RNAs, as was also observed by Beckert *et al.* (28). Our data further imply that both domains are structurally linked to each other and tumble together as one unit. Only the terminal residues and loop regions display increased motion. The inter-domain linker is rather enriched with hydrophobic residues that fold into an α-helix structure, inducing linker rigidity. The preceding residues G263, E264 and D265 are, however, more flexible. Also, the temperature-dependence of rS1–D34 amide resonances hint towards structural transitions within this linker region, suggesting that it might serve as a hinge for correctly positioning both domains for their cellular tasks.

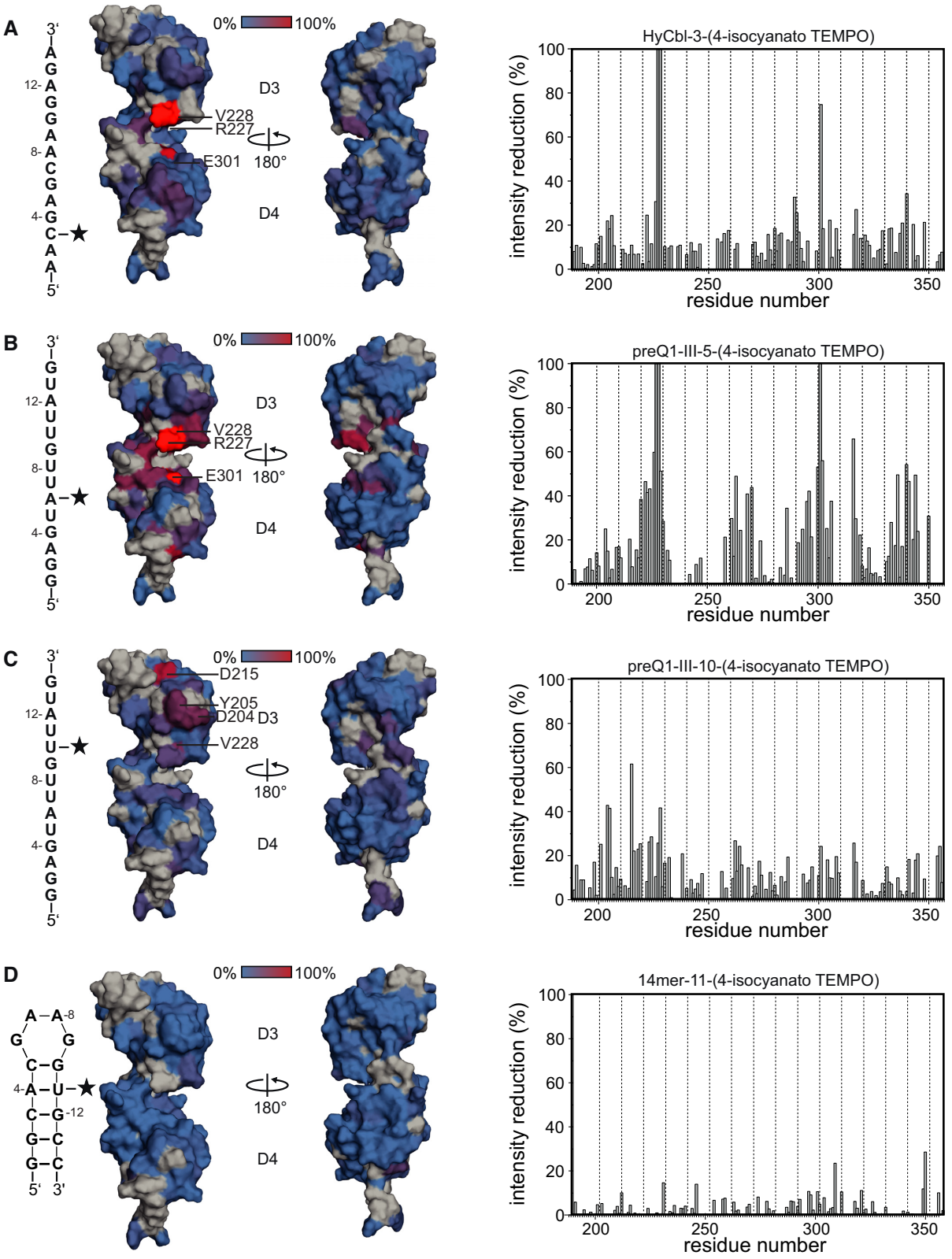

Figure 4. Percentage intensity reductions of paramagnetic samples relative to the diamagnetic reference. All samples contained rS1–D34 and four equivalents of RNA, while the paramagnetic samples were spiked with 10% spin-labeled RNA. Strong changes are highlighted from blue to red in the 3D structure. Overlapping peaks were excluded from the intensity plots and are shown in gray in the 3D structure. Most affected residues are annotated.

It is being recognized that rS1 might also play a role in the translation-regulation mechanism of riboswitches. By use of its chaperoning function rS1 probably modulates folding and dynamics of the riboswitch at the ribosome (21). Thus, we investigated the RNA-recognition capabilities of rS1–D34 with different SD regions mainly stemming from translational riboswitches. We find that rS1 binds the different RNAs with similar affinities (5–30 μM K_D), which is in line with its function to recognize miscellaneous mRNAs for translation initiation. Also, consistent with this is the finding that rS1–D34 preferentially binds to single-stranded RNAs, whereas binding to highly structured regions (G-quadruplex and model hairpin) is not observed under our experimental conditions that exceed the cellular concentrations of RNA significantly. Given the fact that riboswitches are intricately structured 5′-UTR's that exploit structural transitions to signal concentration variations of recognized metabolites, it is pivotal that the translation machinery does not fully destroy this regulation function but rather fine-tunes the execution of it. In our study, we do not observe direct correlation of SD-strength on the binding affinity. Guanines that are enriched in strong SD sequences can be exchanged by adenines without modulating dissociation constants. However, the presence of pyrimidines probably increases RNA binding affinities of rS1 because this smaller nucleobase can be easier accommodated in the RNA binding pocket of rS1. Consequently, binding is driven by the size of the nucleobase and the low propensity of secondary structures.

The affinity regime of the rS1-RNA interaction renders the complex a difficult target for in-depth structural studies by NMR since the complex associate and dissociate in NOE-based experiments. Moreover, the intermediate to fast exchange dynamics observed herein lead to signal-broadening of interacting amino acids, even more obstructing evaluation of protein-RNA contacts at atomic resolution. In fact, in its single-stranded conformation the RNA presumably samples different states, contributing to overall fuzziness of the protein-RNA complex. Therefore, only a rather low-resolution interaction surface can be derived by chemical shift mapping and information for the RNA binding mode remains elusive. Our PRE approach offers a new avenue to enhance structural information on an intermediate-exchanging system. This method enables interpretation of PRE experiments, as it avoids exchange-induced line-broadening. The spiking of RNA with sub-stoichiometric amounts of spin-labeled RNA yields PRE data that can be faithfully analyzed, while at the same time bleaching effects induced by the spin-label are not observed. Moreover, using position-specific spin-labeling in a stepwise manner, the RNA can be utilized as a molecular ruler that provides qualitative information about the relative position and the orientation of the RNA in the protein-RNA complex.

By combining chemical shift mapping and PRE data the following picture for the rS1-RNA interaction emerges: The minimal mRNA binding rS1 construct binds RNAs using positively charged and aromatic amino acids. Positively charged amino acids such as arginines interact with the negatively charged sugar-phosphate backbone of the RNA. The aromatic residues interact with nucleobases, which leads to a melting of base pairs within the RNA. Similar findings were also observed for the *E. coli* cold shock protein CspA, a close relative of OB fold proteins (54). In fact, Renella *et al.* observed that mutations of phenylalanine to isoleucine residues were detrimental for the CspA RNA chaperone activity. The involvement of positively charged and aromatic residues leads to non-specific and transient interactions, resulting in a rather dynamic protein-RNA complex. In fact, for CspA similar RNA-binding affinities were found ($K_D = 12 \pm 2$ μM) as observed herein, indicating that transient interactions are a common feature of OB fold proteins. Such a dynamic interaction is of course important for an RNA chaperone like rS1, as it has to bind and subsequently release different RNA targets in order to execute its chaperoning function. The herein observed interaction regime, however, does not allow a high-resolution NMR structure for the complex of the RNA with rS1. Nevertheless, low-resolution insights can be obtained by chemical shift mapping pinpointing towards the interacting residues. The RNA binding site is confined to one side of the protein, involving the β2-β3-β5 interface within both domains. The PRE approach on the other hand further narrows down the binding site, as the PRE of the spin-label leads to highly local intensity variations. Careful selection of spin-labeling position allows localization of the RNA on to the protein surface with higher resolution and provides further insights on the binding mode. As for rS1–D34 the RNAs are bound with standard polarity by the two OB fold domains, where the 3′-end of the RNA is placed close to the N-terminus of the protein. We can deduce that each S1 domain is capable of binding ∼ 7nt, out of which probably 5–6 nt make direct contact to the RNA binding surface and the inter-domain linker can likely accommodate 1–2 nt. As for the location of the SD region on the rS1 domains, the dynamic nature of the rS1-mRNA interaction likely enables sliding of the RNA on the protein surface, by which the location of the SD region might be diffuse when other 30S-mRNA interactions are absent. The work described here highlights the need to map transient and dynamic parts associated to the ribosome. As demonstrated, this is particular important to understand cis-acting regulatory elements located in the 5′-UTR. The novel NMR tools to map transient interaction surfaces developed in this contribution will be of importance for other RNA–protein complexes.

DATA AVAILABILITY

Atomic coordinates for the reported NMR structure have been deposited with the Protein Data bank under accession number 7A05. Assigned chemical shifts for rS1-34 have been deposited under BMRB accession code 34549.

SUPPLEMENTARY DATA

Supplementary Data are available at NAR Online.

ACKNOWLEDGEMENTS

We thank Christian Richter and Sven Warhaut for help and insightful discussions. We further thank Elke Stirnal and Kerstin Witt for excellent technical assistance.

FUNDING

German funding agency (DFG) in Collaborative Research Center 902: Molecular principles of RNA-based regulation; R.S. is a recipient of a stipend of the Fonds der Chemischen Industrie; E.C. was supported by a stipend of the Polytechnische Gesellschaft; H.R.A. Jonker is supported by DFG in Forschergruppe FOR2509; H.S. and B.F. are supported by the DFG in graduate school CLIC [GRK 1986]; Work at BMRZ was supported by the state of Hesse. Funding for open access charge: Goethe University Frankfurt.
Conflict of interest statement. None declared.

REFERENCES

1. Schmeing,T.M. and Ramakrishnan,V. (2009) What recent ribosome structures have revealed about the mechanism of translation. *Nature*, **461**, 1234–1242.
2. Steitz,T.A. (2008) A structural understanding of the dynamic ribosome machine. *Nat. Rev. Mol. Cell Biol.*, **9**, 242–253.
3. Schuwirth,B.S., Borovinskaya,M.A., Hau,C.W., Zhang,W., Vila-Sanjurjo,A., Holton,J.M. and Cate,J.H.D. (2005) Structures of the bacterial ribosome at 3.5 A resolution. *Science*, **310**, 827–834.
4. Selmer,M., Dunham,C.M., Murphy,F.V, Weixlbaumer,A., Petry,S., Kelley,A.C., Weir,J.R. and Ramakrishnan,V. (2006) Structure of the 70S ribosome complexed with mRNA and tRNA. *Science*, **313**, 1935–1942.
5. Korostelev,A., Trakhanov,S., Laurberg,M. and Noller,H.F. (2006) Crystal structure of a 70S ribosome-tRNA complex reveals functional interactions and rearrangements. *Cell*, **126**, 1065–1077.
6. Ogle,J.M., Brodersen,D.E., Clemons,W.M., Tarry,M.J., Carter,A.P. and Ramakrishnan,V. (2001) Recognition of cognate transfer RNA by the 30S ribosomal subunit. *Science*, **292**, 897–902.
7. Nissen,P., Hansen,J., Ban,N., Moore,P.B. and Steitz,T.A. (2000) The structural basis of ribosome activity in peptide bond synthesis. *Science*, **289**, 920–930.
8. Martin Schmeing,T., Huang,K.S., Strobel,S.A. and Steitz,T.A. (2005) An induced-fit mechanism to promote peptide bond formation and exclude hydrolysis of peptidyl-tRNA. *Nature*, **438**, 520–524.
9. Schmeing,T.M., Huang,K.S., Kitchen,D.E., Strobel,S.A. and Steitz,T.A. (2005) Structural insights into the roles of water and the 2′ hydroxyl of the P site tRNA in the peptidyl transferase reaction. *Mol. Cell*, **20**, 437–448.
10. Schmeing,T.M., Seila,A.C., Hansen,J.L., Freeborn,B., Soukup,J.K., Scaringe,S.A., Strobel,S.A., Moore,P.B. and Steitz,T.A. (2002) A pre-translocational intermediate in protein synthesis observed in crystals of enzymatically active 50S subunits. *Nat. Struct. Biol.*, **9**, 225–230.
11. Suryanarayana,T. and Subramanian,A.R. (1979) Functional domains of *Escherichia coli* ribosomal protein S1. Formation and characterization of a fragment with ribosome-binding properties. *J. Mol. Biol.*, **127**, 41–54.
12. Bycroft,M., Hubbard,T.J.P., Proctor,M., Freund,S.M.V. and Murzin,A.G. (1997) The solution structure of the S1 RNA binding domain: a member of an ancient nucleic acid-binding fold. *Cell*, **88**, 235–242.
13. Draper,D.E. and Reynaldo,L.P. (1999) RNA binding strategies of ribosomal proteins. *Nucleic Acids Res.*, **27**, 381–388.
14. Byrgazov,K., Grishkovskaya,I., Arenz,S., Coudevylle,N., Temmel,H., Wilson,D.N., Djinovic-Carugo,K. and Moll,I. (2015) Structural basis for the interaction of protein S1 with the Escherichia coli ribosome. *Nucleic Acids Res.*, **43**, 661–673.
15. Boni,I.V, Lsaeva,D.M., Musychenko,M.L. and Tzareva,N.V. (1991) Ribosome-messenger recognition: mRNA target sites for ribosomal protein S1. *Nucleic Acids Res.*, **19**, 155–162.
16. Komarova,A.V., Tchufistova,L.S., Dreyfus,M. and Boni,I.V. (2005) AU-rich sequences within 5′ untranslated leaders enhance translation and stabilize mRNA in *Escherichia coli*. *J. Bacteriol.*, **187**, 1344–1349.
17. Qu,X., Wen,J.D, Lancaster,L., Noller,H.F., Bustamante,C. and Tinoco,I. (2011) The ribosome uses two active mechanisms to unwind messenger RNA during translation. *Nature*, **475**, 118–121.
18. Qureshi,N.S., Bains,J.K., Sreeramulu,S., Schwalbe,H. and Fürtig,B. (2018) Conformational switch in the ribosomal protein S1 guides unfolding of structured RNAs for translation initiation. *Nucleic Acids Res.*, **46**, 10917–10929.
19. Shine,J. and Dalgarno,L. (1974) The 3′-terminal sequence of *Escherichia coli* 16S ribosomal RNA: complementarity to nonsense triplets and ribosome binding sites. *Proc. Natl. Acad. Sci. USA*, **71**, 1342–1346.
20. Duval,M., Korepanov,A., Fuchsbauer,O., Fechter,P., Haller,A., Fabbretti,A., Choulier,L., Micura,R., Klaholz,B.P., Romby,P. *et al.* (2013) *Escherichia coli* ribosomal protein S1 unfolds structured mRNAs onto the ribosome for active translation initiation. *PLoS Biol.*, **11**, 12–14.
21. Ray,S., Chauvier,A. and Walter,N.G. (2019) Kinetics coming into focus: single-molecule microscopy of riboswitch dynamics. *RNA Biol.*, **16**, 1077–1085.
22. Sørensen,M.A., Fricke,J. and Pedersen,S. (1998) Ribosomal protein S1 is required for translation of most, it not all, natural mRNAs in *Escherichia coli* in vivo. *J. Mol. Biol.*, **280**, 561–569.
23. Loveland,A.B. and Korostelev,A.A. (2017) Structural dynamics of protein S1 on the 70S ribosome visualized by ensemble cryo-EM. *Methods*, **137**, 55–66.
24. Demo,G., Rasouly,A., Vasilyev,N., Svetlov,V., Loveland,A.B., Diaz-Avalos,R., Grigorieff,N., Nudler,E. and Korostelev,A.A. (2017) Structure of RNA polymerase bound to ribosomal 30S subunit. *Elife*, **6**, e28560.
25. Takeshita,D., Yamashita,S. and Tomita,K. (2014) Molecular insights into replication initiation by Qβ replicase using ribosomal protein S1. *Nucleic Acids Res.*, **42**, 10809–10822.
26. Kidmose,R.T., Vasiliev,N.N., Chetverin,A.B., Andersen,G.R. and Knudsen,C.R. (2010) Structure of the Qbeta replicase, an RNA-dependent RNA polymerase consisting of viral and host proteins. *Proc. Natl. Acad. Sci. U.S.A.*, **107**, 10884–10889.
27. Salah,P., Bisaglia,M., Aliprandi,P., Uzan,M., Sizun,C. and Bontems,F. (2009) Probing the relationship between gram-negative and gram-positive S1 proteins by sequence analysis. *Nucleic Acids Res.*, **37**, 5578–5588.
28. Beckert,B., Turk,M., Czech,A., Berninghausen,O., Beckmann,R., Ignatova,Z., Plitzko,J.M. and Wilson,D.N. (2018) Structure of a hibernating 100S ribosome reveals an inactive conformation of the ribosomal protein S1. *Nat. Microbiol.*, **3**, 1115–1121.
29. Schiemann,O., Piton,N., Mu,Y., Stock,G., Engels,J.W. and Prisner,T.F. (2004) A PELDOR-based nanometer distance ruler for oligonucleotides. *J. Am. Chem. Soc.*, **126**, 5722–5729.
30. Ramos,A. and Varani,G. (1998) A new method to detect long-range protein-RNA contacts: NMR detection of electron-proton relaxation induced by nitroxide spin-labeled RNA [9]. *J. Am. Chem. Soc.*, **120**, 10992–10993.
31. Edwards,T.E. and Sigurdsson,S.T. (2007) Site-specific incorporation of nitroxide spin-labels into 2′ -positions of nucleic acids. *Nat. Protoc.*, **2**, 1954–1962.
32. Wishart,D.S., Bigam,C.G., Yao,J., Abildgaard,F., Dyson,H.J., Oldfield,E., Markley,J.L. and Sykes,B.D. (1995) 1H, 13C and 15N chemical shift referencing in biomolecular NMR. *J. Biomol. NMR*, **6**, 135–140.
33. Goddard,T.D. and Kneller,D.G. (2008) SPARKY 3.
34. Solyom,Z., Schwarten,M., Geist,L., Konrat,R., Willbold,D. and Brutscher,B. (2013) BEST-TROSY experiments for time-efficient sequential resonance assignment of large disordered proteins. *J. Biomol. NMR*, **55**, 311–321.
35. Lescop,E., Schanda,P. and Brutscher,B. (2007) A set of BEST triple-resonance experiments for time-optimized protein resonance assignment. *J. Magn. Reson.*, **187**, 163–169.
36. Favier,A. and Brutscher,B. (2011) Recovering lost magnetization: polarization enhancement in biomolecular NMR. *J. Biomol. NMR*, **49**, 9–15.
37. Dosset,P., Hus,J.C., Blackledge,M. and Marion,D. (2000) Efficient analysis of macromolecular rotational diffusion from heteronuclear relaxation data. *J. Biomol. NMR*, **16**, 23–28.
38. García De La Torre,J., Huertas,M.L. and Carrasco,B. (2000) Calculation of hydrodynamic properties of globular proteins from their atomic-level structure. *Biophys. J.*, **78**, 719–730.

39. Williamson,M.P. (2013) Using chemical shift perturbation to characterise ligand binding. *Prog. Nucl. Magn. Reson. Spectrosc.*, **73**, 1–16.
40. Iwahara,J., Tang,C. and Marius Clore,G. (2007) Practical aspects of 1H transverse paramagnetic relaxation enhancement measurements on macromolecules. *J. Magn. Reson.*, **184**, 185–195.
41. Güntert,P. (2003) Automated NMR protein structure calculation. *Prog. Nucl. Magn. Reson. Spectrosc.*, **43**, 105–125.
42. Güntert,P. (2004) Automated NMR structure calculation with CYANA. In: *Protein NMR Techniques*. Humana Press, New Jersey, pp. 353–378.
43. Shen,Y. and Bax,A. (2013) Protein backbone and sidechain torsion angles predicted from NMR chemical shifts using artificial neural networks. *J. Biomol. NMR*, **56**, 227–241.
44. Linge,J.P., Williams,M.A., Spronk,C.A.E.M., Bonvin,A.M.J.J. and Nilges,M. (2003) Refinement of protein structures in explicit solvent. *Proteins Struct. Funct. Bioinforma.*, **50**, 496–506.
45. Zweckstetter,M. and Bax,A. (2000) Prediction of sterically induced alignment in a dilute liquid crystalline phase: aid to protein structure determination by NMR [11]. *J. Am. Chem. Soc.*, **122**, 3791–3792.
46. Biasini,M., Bienert,S., Waterhouse,A., Arnold,K., Studer,G., Schmidt,T., Kiefer,F., Cassarino,T.G., Bertoni,M., Bordoli,L. *et al.* (2014) SWISS-MODEL: modelling protein tertiary and quaternary structure using evolutionary information. *Nucleic Acids Res.*, **42**, W252–W258.
47. Holmstrom,E.D., Polaski,J.T., Batey,R.T. and Nesbitt,D.J. (2014) Single-molecule conformational dynamics of a biologically functional hydroxocobalamin riboswitch. *J. Am. Chem. Soc.*, **136**, 16832–16843.
48. Rinaldi,A.J., Lund,P.E., Blanco,M.R. and Walter,N.G. (2016) The Shine-Dalgarno sequence of riboswitch-regulated single mRNAs shows ligand-dependent accessibility bursts. *Nat. Commun.*, **7**, 8976.
49. Chauvier,A., Picard-Jean,F., Berger-Dancause,J.C., Bastet,L., Naghdi,M.R., Dubé,A., Turcotte,P., Perreault,J. and Lafontaine,D.A. (2017) Transcriptional pausing at the translation start site operates as a critical checkpoint for riboswitch regulation. *Nat. Commun.*, **8**,13892.
50. Liberman,J.A., Suddala,K.C., Aytenfisu,A., Chan,D., Belashov,I.A., Salim,M., Mathews,D.H., Spitale,R.C., Walter,N.G. and Wedekind,J.E. (2015) Structural analysis of a class III preQ $_1$ riboswitch reveals an aptamer distant from a ribosome-binding site regulated by fast dynamics. *Proc. Natl. Acad. Sci.*, **112**, E3485–E3494.
51. Lipecky,R., Kohlschein,J. and Gassen,H.G. (1977) Complex formation between ribosomal protein S1, oligo-and polynucleotides: chain length dependence and base specificity. *Nucleic Acids Res.*, **4**, 3627–3642.
52. Cetiner,E.C. and Schwalbe,H. (2018) Chapter 9. Paramagnetic NMR in drug discovery. In: Luchinat,C., Parigi,G. and Ravera,E. (eds). *New Developments in NMR*. Royal Society of Chemistry, Cambridge, pp. 258–282.
53. Theobald,D.L., Mitton-Fry,R.M. and Wuttke,D.S. (2003) Nucleic acid recognition by OB-fold proteins. *Annu. Rev. Biophys. Biomol. Struct.*, **32**, 115–133.
54. Rennella,E., Sára,T., Juen,M., Wunderlich,C., Imbert,L., Solyom,Z., Favier,A., Ayala,I., Weinhäupl,K., Schanda,P. *et al.* (2017) RNA binding and chaperone activity of the E. coli cold-shock protein CspA. *Nucleic Acids Res.*, **45**, 4255–4268.